137 (2022) 212823

Contents lists available at ScienceDirect

Biomaterials Advances

journal homepage: www.journals.elsevier.com/materials-science-and-engineering-c

Synthesis of a theranostic platform based on fibrous silica nanoparticles for the enhanced treatment of triple-negative breast cancer promoted by a combination of chemotherapeutic agents

Karina Ovejero-Paredes [a,b], Diana Díaz-García [c], Irene Mena-Palomo [c], Marzia Marciello [a], Laura Lozano-Chamizo [a,b], Yurena Luengo Morato [a], Sanjiv Prashar [c], Santiago Gómez-Ruiz [c,*], Marco Filice [a,b,d,**]

[a] *Nanobiotechnology for Life Sciences Group, Department of Chemistry in Pharmaceutical Sciences, Faculty of Pharmacy, Universidad Complutense de Madrid (UCM), Plaza Ramón y Cajal s/n, E-28040 Madrid, Spain*
[b] *Microscopy and Dynamic Imaging Unit, Fundación Centro Nacional de Investigaciones Cardiovasculares Carlos III (CNIC), Calle Melchor Fernandez Almagro 3, E-28029 Madrid, Spain*
[c] *COMET-NANO Group, Department of Biology and Geology, Physics and Inorganic Chemistry, ESCET, Universidad Rey Juan Carlos, Calle Tulipán s/n, E-28933 Móstoles, Madrid, Spain*
[d] *CIBER de Enfermedades Respiratorias (CIBERES), Melchor Fernández Almagro, 3, 28029 Madrid, Spain*

ARTICLE INFO

Keywords:
Multifunctional silica nanoparticles
Cancer theranosis
Triple negative breast cancer
Molecular imaging
Pharmaceutical chemistry
Nanobiotechnology

ABSTRACT

A new series of theranostic silica materials based on fibrous silica particles acting as nanocarriers of two different cytotoxic agents, namely, chlorambucil and an organotin metallodrug have been prepared and structurally characterized. Besides the combined therapeutic activity, these platforms have been decorated with a targeting molecule (folic acid, to selectively target triple negative breast cancer) and a molecular imaging agent (Alexa Fluor 647, to enable their tracking both *in vitro* and *in vivo*). The *in vitro* behaviour of the multifunctional silica systems showed a synergistic activity of the two chemotherapeutic agents in the form of an enhanced cytotoxicity against MDA-MB-231 cells (triple negative breast cancer) as well as by a higher cell migration inhibition. Subsequently, the *in vivo* applicability of the siliceous nanotheranostics was successfully assessed by observing with *in vivo* optical imaging techniques a selective tumour accumulation (targeting ability), a marked inhibition of tumour growth paired to a marked antiangiogenic ability after 13 days of systemic administration, thus, confirming the enhanced theranostic activity. The systemic nanotoxicity was also evaluated by analyzing specific biochemical markers. The results showed a positive effect in form of reduced cytotoxicity when both chemotherapeutics are administered in combination thanks to the fibrous silica nanoparticles. Overall, our results confirm the promising applicability of these novel silica-based nanoplatforms as advanced drug-delivery systems for the synergistic theranosis of triple negative breast cancer.

1. Introduction

Worldwide, one of the most common cause of death in women is breast cancer [1–3], and more specifically, triple-negative breast cancer (TNBC). This type of tumour does not express the estrogen receptor (ER), the human epidermal receptor 2 (HER2) and the progesterone receptor (PR). It is associated with around 20% of newly diagnosed breast cancers, with a very bad prognosis and poor survival rate due its aggressive nature and very high potential to promote metastasis [4,5].

Currently, there are some chemotherapeutic drugs for the treatment of breast cancer, which help in the suppression or reduction of cancer cell growth [1,6–9]. In this context, chlorambucil (*N*,*N*-bis(2-chloroethyl)-*p*-aminophenylbutyric acid (Chl)), is a well-known anticancer drug considered as a DNA alkylating agent with a high potential against

* Correspondence to: Prof. S. Gómez-Ruiz, COMET-NANO Group, Department of Biology and Geology, Physics and Inorganic Chemistry, ESCET, Universidad Rey Juan Carlos, Calle Tulipán s/n, E-28933 Móstoles, Madrid, Spain.
** Correspondence to: Prof. M. Filice, Nanobiotechnology for Life Sciences Group, Dept of Chemistry in Pharmaceutical Sciences, Faculty of Pharmacy, Universidad Complutense de Madrid (UCM), Plaza Ramón y Cajal s/n, E-28040 Madrid, Spain.
E-mail addresses: santiago.gomez@urjc.es (S. Gómez-Ruiz), mfilice@ucm.es (M. Filice).

https://doi.org/10.1016/j.bioadv.2022.212823
Received 12 December 2021; Received in revised form 3 April 2022; Accepted 20 April 2022
Available online 25 April 2022

different tumours, including breast cancer [1,10–13]. This drug acts by a mechanism that is based on straightforward binding to specific sites of DNA (N7 of guanine or adenine and N3 of adenine) [14–16]. Nevertheless, the therapeutic effect of chlorambucil is restricted because of its toxicity and associated adverse effects at high doses [17,18]. Therefore, chlorambucil is always used in very low doses and this reduces the effectivity of the therapeutic treatment [19]. In addition, in preclinical stage, metallodrugs such as organotin(IV) derivatives have been successfully used against TNBC, although they also showed some toxic side effects [20].

Therefore, although some therapeutic agents have potential to be used against TNBC, the lack of molecular targets which allow recognition of this type of tumour, poses huge challenges to oncologists [21]. To tackle this issue, the folate receptor alpha has been employed as a molecular target because these fragments are usually overexpressed in a wide variety of breast tumours [22–24], including the cells causing TNBC, MDA-MB-231 [25–28]. Thus, effective targeting and al a fine combination of different drugs in low doses for TNBC treatment represents a powerful alternative able to reduce the toxicity while maintaining anticancer activity.

In several cases, an entrapment of therapeutic agents within an appropriate drug delivery system [29–34] has become very important in reducing harmful side effects, increasing drug bioavailability and pharmacokinetic and enhancing drug accumulation into the target zone. Nanomaterials have shown great usefulness as suitable vectors for drug delivery in general [35] and for metallodrugs and chlorambucil delivery in particular [36–41] due to their intrinsic properties, their ability to reduce drug degradation and improve its specificity and therapeutic activity.

Beside the therapeutic aspect, an early and facile diagnostic is also very important goal in many diseases, especially in cancer [42]. Therefore, an interesting and appropriate delivery system should combine therapeutic (drugs) with diagnostic (molecular imaging fragments) moieties at the same time, thus, enabling so called theranosis (*therapy* + *diagnosis*). Due to its tremendous potential, this multifunctional therapeutic approach has gained momentum within the medical community as underlined very recently in the cited reports [43,44]. Due to their special characteristics, nanomaterials offer a plethora of possibilities for cancer theranosis [37,45].

Within all the possibilities, nanomaterials of silica have been largely employed in biomedicine [41,46–52] for different purposes such as imaging (fluorescence and magnetic resonance imaging) [53], therapeutic controlled release of drugs [54–60] or imaging and therapy, as in the case of theranostics [20,48,61–65]. One of the most interesting variants of nanostructured silicas are the fibrous particles also called “wrinkled” silicas. This type of materials has recently gained the attention of the scientific community due to their great benefits, such as, a simple synthetic procedure, tunable internal structure and morphology, and a good capacity of functionalization. Fibrous silica particles have similar chemical and morphological characteristics to those of typical mesoporous silica nanoparticles (MSN). However, the particular structure of fibrous systems allows a better interaction with the cell membrane in biological environments, as the fibrous topography improves the cellular uptake by interacting actively with the membrane mechanics [66]. Moreover, it has also been reported that the roughness in the particle surface reduces the unspecific adsorption of proteins - in comparison with smooth surface particles, thus reducing the formation of protein corona [67]. In addition, its radially distributed fibrous channels usually promote an increase in the functionalization capacity due to the existence of many accessible sites, which permit an easy incorporation of different agents. This allows the design and preparation of different multimodal systems for biomedical applications [68,69]. Thanks to these advantages, fibrous silica nanostructured systems can be designed to be multifunctional, for example, being capable of exerting simultaneously therapeutic and diagnostic activity along with a targeting system.

Consequently, considering the possibility of multiple decoration by using various cytotoxic agents, molecular imaging contrast agents and a site-selective targeting moiety all in a single entity, we have envisaged the fibrous nanostructured silica as a promising synergistic nanoplatform for cancer theranosis.

In this study, the synthesis and characterization of a new silica-based fibrous theranostic nanocarrier bearing two different therapeutic agents (organotin(IV) complex and chlorambucil), a targeting moiety (folic acid) and diagnostic contrast agent (Alexa Fluor 647) is described. After a thorough physical and chemical characterization, the applicability and viability of these nanodrugs was assessed *in vitro* against different cell lines. Subsequently, the theranostic ability as well as the toxicity of the fibrous nanoplatforms was evaluated *in vivo* using orthotopic xenograft TNBC murine models.

2. Materials and methods

2.1. Reagents

All functionalization reactions, except the 1-ethyl-3-(3-dimethylaminopropyl)carbodiimide EDAC-assisted amido formation, were carried out under an inert atmosphere of dry nitrogen using Schlenk techniques. Toluene and triethylamine were distilled from the appropriate drying agents and degassed before use. For the preparation of the silica material (FSP), cetylpyridinium bromide hydrate (CPB), tetraethyl orthosilicate (TEOS), and urea, (Sigma Aldrich) were used. The chemical reagents, 3-mercaptopropyltriethoxysilane (MP, Fluorochem), trimethoxysilylpropyldiethylenetriamine (DT, Fluorochem), triphenyltin chloride (Sigma Aldrich), were used for the functionalization of fibrous silica materials. EDAC, 2-(N-morpholino)ethanesulfonic acid (MES), N-hydroxysuccinimide (NHS), folic acid (FA) and chlorambucil (Chl), purchased from Sigma Aldrich and Fluorochem, respectively, were used in the amido coupling reactions. The Alexa Fluor 647 Succinimidyl Ester (AX) dye was supplied by Thermofisher. All compounds were employed directly without further purification. MDA-MB-231 cells were from ATCC. The 3-(4,5-dimethylthiazol-2-yl)-2,5-diphenyltetrazolium bromide (MTT) reagent for cell viability assay was purchased from Sigma-Aldrich. For cell culture reagents: Dulbecco's Modified Eagle Medium-Nutrient Mixture F-12 (DMEM-F12, Lonza, Basel, Switzerland) and penicillin/streptomycin were purchased from Lonza (Basel, Switzerland), fetal bovine serum (FBS) was purchased from Sigma Aldrich (St. Louis, MO, USA), TrypLE™ Express Enzyme from Gibco, and non-essential amino acids (NEAA) and sodium pyruvate were purchased from Hyclone (South Logan, UT, USA).

2.2. Synthesis and functionalization of fibrous silica particles (FS)

2.2.1. Synthesis of fibrous silica particles (FS)

The fibrous silica particles (**FS**) were synthesized following the method published by Sadeghzadeh et al. [70], introducing slight modifications. In summary, **FS** was prepared as follows: 1 g (2.60 mmol) of CPB was dissolved in 60 mL Milli-Q water, then 1.2 g (19.98 mmol) of urea was added. The mixture was rigorously stirred for 15 min. Subsequently, a solution of 5 mL (22.39 mmol) of TEOS in a mixture of cyclohexane and 1-pentanol (60 mL : 3 mL) was added dropwise with an addition funnel, and the mixture was stirred for 45 min and then was transferred to a hydrothermal reactor at 120 °C for 5 h. The resulting white solid was isolated by filtration, washed with abundant Milli-Q water and methanol, and dried in a stove. Finally, the silica was calcined at 550 °C for 24 h.

2.2.2. Functionalization with DT ligand

For the synthesis of **FS-DT** derivative, 2 g of the **FS** starting material were dried overnight at 80 °C and under vacuum. The particles were then dispersed in 30 mL of dry toluene and 3.88 mL (12.06 mmol) of trimethoxysilyl-propyldiethylenetriamine (DT) was added. The solution

was kept under stirring at 80 °C for 48 h. Afterwards, the suspension was centrifuged (6000 rpm, 10 min), and the isolated solid washed with toluene and diethylether, and dried in a stove.

2.2.3. Incorporation of chlorambucil and targeting agent

The reaction of functionalization of the nanostructured material with chlorambucil (Chl, chemotherapeutic agent 1) and folic acid (FA, targeting agent), a carbodiimide coupling reaction was promoted. In summary, 180 mg (0.59 mmol) of Chl and 180 mg (0.41 mmol) of FA (10% functionalization w/w SiO_2/Chl and FA) were dissolved in dimethylsulfoxide (DMSO) with the help of an ultrasonic bath at room temperature, and the solution was then added to 180 mL of MES buffer solution (pH 6.0) prepared by mixing 72 mg (0.38 mmol) of EDAC and 108 mg (0.94 mmol) of NHS. The resulting mixture was stirred at room temperature for 15 additional minutes and, subsequently, 315 μL of 2-mercaptoethanol (4.49 mmol) was added dropwise to the solution. Afterwards, 1.8 g of DT-functionalized FS nanoparticles was added to the EDAC solution and allowed to react for 2 additional hours at room temperature under vigorous magnetic stirring. Finally, the mixture was centrifuged and the isolated solid washed with DMSO, Milli-Q water and ethanol and dried in a stove. The final product was labelled as **FS-DT-Chl-FA**. In order to study the activity of chlorambucil and folic acid, the materials **FS-DT-FA** and **FS-DT-Chl** were synthesized in an analogous way.

2.2.4. Functionalization with organotin(IV) compound

For the functionalization with the metallodrug, the first step was the preparation of the compound $Ph_3Sn\{SCH_2CH_2CH_2Si(OEt)_3\}$ (Sn, chemotherapeutic agent 2), which was carried out by reacting triphenyltin(IV) chloride with 3-mercaptopropyltrimethoxysilane (Scheme S1), In a Schlenk tube, $SnPh_3Cl$ (180.4 mg, 0.47 mmol) was dissolved in 20 mL of dry toluene in a proportion of 10 wt.% Sn/SiO_2. In a second step, 3-mercaptopropyltriethoxysilane (113.1 μL, 0.47 mmol) and triethylamine (130.5 μL, 0.94 mmol) were added. The suspension was then stirred under inert atmosphere for 24 h at 110 °C. The reaction mixture was then filtered with a filter cannula and the filtrate was then transferred to a toluene suspension of 500 mg of silica material (**FS-DT**, **FS-DT-FA**, **FS-DT-Chl** or **FS-DT-Chl-FA**). The resulting suspension was stirred at 110 °C for 24 h. The final material was isolated by filtration and washed several times with toluene and ethanol.

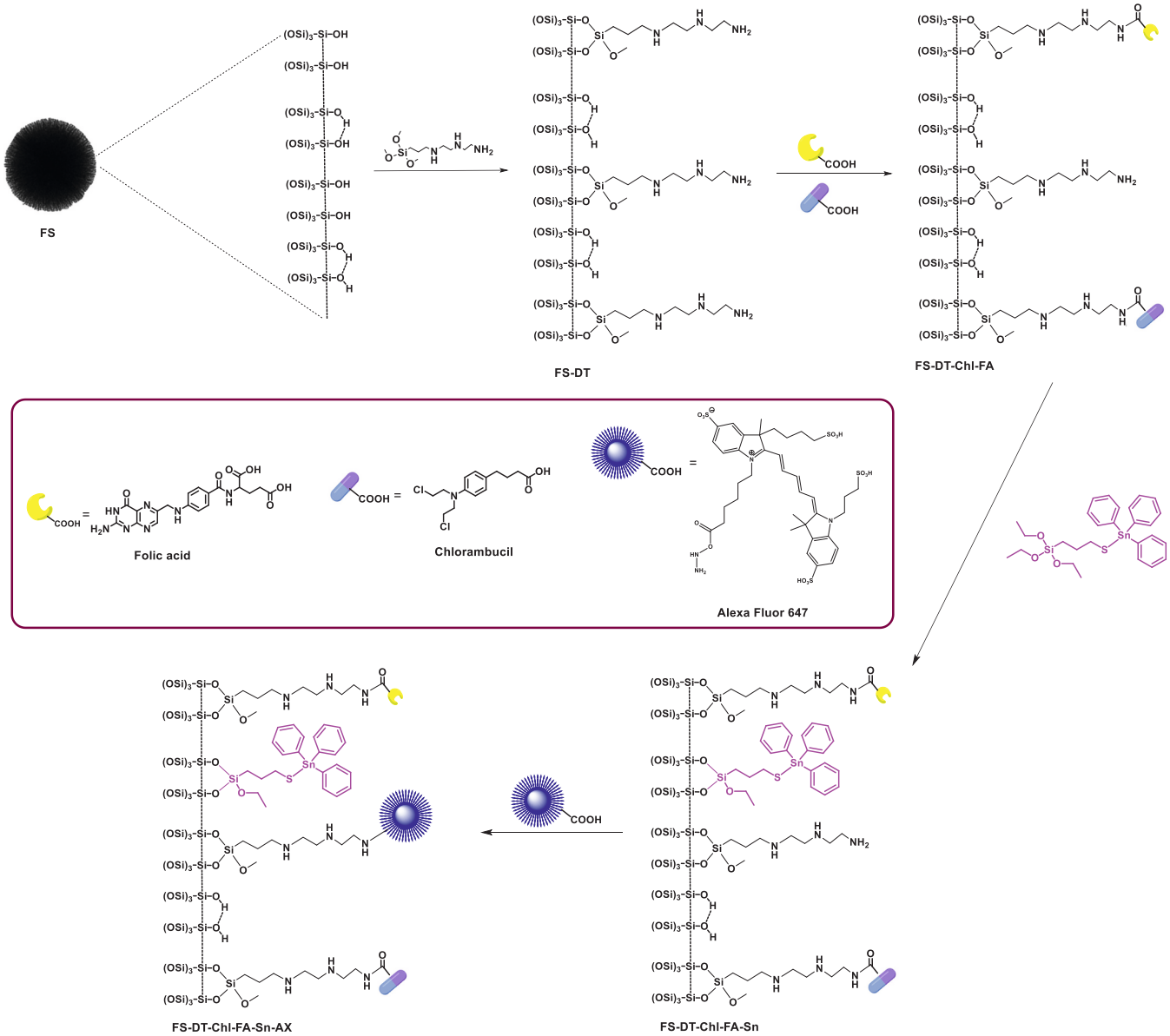

Scheme 1. General scheme of the synthesis of the theranostic platform **FS-DT-Chl-FA-Sn-AX** based on fibrous silica nanoparticles.

2.2.5. Incorporation of the imaging agent Alexa Fluor 647 succinimidyl ester (AX)

50 μg of the fluorophore was dissolved in 100 μL of dimethylsulfoxide (DMSO) and the solution was added to 50 mg of the silica materials **FS-DT-FA**, **FS-DT-FA-Sn** and **FS-DT-Chl-FA-Sn**, dispersed in 5 mL of 0.1 M $NaHCO_3$ buffer (pH 8.2). The suspension was stirred in the dark at room temperature for 1 h. Finally, the solid was isolated by centrifuge and washed with DMSO and water, obtaining the final materials **FS-DT-FA-AX**, **FS-DT-FA-Sn-AX** and **FS-DT-Chl-FA-Sn-AX** (Scheme 1).

2.3. Physicochemical characterization of nanomaterials

Transmission electron microscopy (TEM) was carried out with the model JEOL JEM 1010, operating at 100 kV and the micrographs were analyzed using the program ImageJ. FT-IR spectra analysis was carried out with a spectrophotometer Termo Nicolet Avatar 380 FT-IR with a Michelson filter interferometer with samples prepared using KBr pellets. X-ray fluorescence (XRF) characterization was carried out with a Philips MagiX spectrophotometer with an X-ray source of 1 kW and a Rh anode using a helium atmosphere. Thermogravimetric analyses (TG) were obtained with a Shimadzu mod. DSC-50Q operating between 30 and 950 °C (ramp 20 °C/min) at an intensity of 50 A in nitrogen. N_2 gas adsorption–desorption isotherms were performed using a Micromeritics ASAP 2020 analyzer. ^{29}Si magic angle spinning nuclear magnetic resonance (^{29}Si MAS NMR) and ^{13}C Cross-Polarization (^{13}C-CP) spectra, were recorded on a Varian-Infinity Plus Spectrometer at 400 MHz operating at 100.52 MHz proton frequency (4 μs 90° pulse, 4000 transients, spinning speed of 6 MHz, contact time 3 ms, pulse delay 1.5 s). ICP-AES studies were carried out on a Varian Vista AX Pro Varian 720-ES (λ (Sn) = 283.998 nm). Hydrodynamic diameter and surface ζ-potential measurements were acquired on a Dynamic Light Scattering (DLS) Zetasizer Nano Zen 3600 (Malvern), diluting samples in potassium nitrate aqueous solution (KNO_3, 0.01 M).

2.4. Release study of tin from multifunctional silica carriers

A tin leaching study was carried out to determine the concentration of the tin-containing soluble species in simulated body fluid. **FS-DT-Chl-FA-Sn** material was used as model in pH 7.4 PBS buffer in duplicate. 5 mg of nanomaterial was added to 5 mL of buffer and the suspension was incubated at 37 °C and 30 rpm, in a Roto-Therm incubator (Benchmark) for 3, 8, 24, 48 and 72 h. Subsequently, the suspension was filtered through a nylon filter (0.2 μm) and the obtained solution was analyzed by ICP-AES in triplicate to determine the quantity of Sn leached in the solution after every cycle.

2.5. In vitro studies

2.5.1. Cell lines and culture condition

The triple-negative human breast adenocarcinoma cell line MDA-MB-231 was cultured in DMEM-F12 supplemented with 10% FBS, 1% non-essential amino acids, 1% sodium pyruvate 100 mM and 1% penicillin/streptomycin. The culture was maintained at 37 °C in a humidified atmosphere with 5% CO_2. The cells were subcultured every 2–3 days by treatment with TrypLE™ Express Enzyme.

2.5.2. Nanodrug preparation

For *in vitro* assays, various suspensions of the nanomaterials at different concentrations were prepared in culture media (without phenol red). The final suspensions were always sonicated repeatedly before cell incubation.

2.5.3. Cell viability assay

1×10^4 MDA-MB-231 cells were seeded per well in a 96-well culture plate for 48 h. After that, cells were incubated 24 h at 37 °C with dispersions of each silica-functionalized material (**FS-DT-Chl-FA**, **FS-DT-FA-Sn** or **FS-DT-Chl-FA-Sn**) in culture medium without phenol red at different final Sn concentrations: 0.1 μM, 0.25 μM, 0.5 μM, 1 μM, 2.5 μM, 5 μM, 10 μM, 25 μM, 50 μM, 100 μM, 150 μM and 200 μM. The concentrations studied for silica materials functionalized with chlorambucil alone were equal to those of the series containing both drugs and quantified by Sn concentration. Once finished the incubation period, the suspensions were removed and replaced by 100 μL of cell culture medium without phenol red and without serum. After that 10 μL of a 12 mM MTT (dimethylthiazolyl-diphenyl-tetrazolium bromide) solution (in PBS 1×, pH 7.4) was added to each well and mixed. After 3 h of incubation, the supernatants were removed with exception of 25 μL, and 100 μL DMSO were added to each well to dissolve the insoluble formazan salt, leaving it 15 min to react. Cell viability was estimated by measuring absorbance at 570 nm using a SPECTROstar Nano UV–Vis plate reader (BMG Labtech).

2.5.4. Wound healing assay

1×10^5 MDA-MB-231 cells per well were seeded in a 24-well culture plate for 48 h, in order to create a uniform cell monolayer. After that, a linear scar was generated on the cellular layer by using a pipette tip, the medium was absorbed with vacuum and the wells were cleaned twice with PBS without Ca or Mg. Finally, the cells were incubated with the different nanomaterials (**FS-DT**, **FS-DT-Chl-FA**, **FS-DT-FA-Sn** or **FS-DT-Chl-FA-Sn**) resuspended in cell culture medium at different concentrations (1 μM, 5 μM, 10 μM and 25 μM) and the gap migration was imaged at 0, 24 and 72 h later using a Nikon Time Lapse microscope.

2.6. In vivo studies

2.6.1. Animals and ethics

Mice were housed in specific facilities (pathogen-free for mice) at the Spanish National Center for Cardiovascular Research (CNIC, Madrid, Spain). All animal experiments were carried out after previous approval by the ethics and animal welfare committee at CNIC and were in agreement with the Spanish Legislation and UE Directive 2010/63/EU.

2.6.2. Breast cancer mouse model

The orthotopic breast cancer was generated by injecting subcutaneously 2×10^6 MDA-MB-231 cells (in a 20 μL mixture of PBS 1× and Matrigel, 1.86:1 v/v) into 9-week-old NOD Scid IL2 receptor gamma chain KO female mice, in their fourth left breast. Animals were housed at 22 °C, under a 12 h light/dark cycle with freely available water and food. The tumour was generally generated within the next 20 days after the injection.

2.6.3. Material administration and in vivo fluorescence imaging

Mice (n = 4/group) were injected i.v. into the tail vein with 150 μL of the materials suspensions (**FS-DT-Chl-FA-AX**, **FS-DT-FA-Sn-AX** and **FS-DT-Chl-FA-Sn-AX**) at fixed concentrations of 420 μM in tin and 320.5 μM in Chlorambucil, over 13 days (6 injections). Two hours post administration, *in vivo* fluorescence follow up of Alexa Fluor 647 was performed on mice anesthetized with isoflurane gas. Murine models with saline treatment were used as control. Fluorescence *in vivo* imaging was performed with IVIS Imaging System 200 series (Xenogen®) (acquisition parameters: Cy5.5 ex/em filter, high level, BIN-HR, FOV: 6.6; f8). The therapeutic regimen as well as the imaging protocol were applied based on previous studies carried out with the same tumour model and similar silica-based nanosystems [20,35,63,71,72].

2.6.4. Tumour measurement

To evaluate the tumour growth, all mice were monitored by caliper measurements of tumour width (W) and length (L). Tumour volume was determined using the formula $V = (L * (W^2)) / 2$ and volumes were normalized and compared with respect to the initial volumes of each studied tumour mass.

2.6.5. Evaluation of antiangiogenic activity at the tumour site

To evaluate the inhibition of the formation of new blood vessels, vascularization images of blood flow of the tumour areas were obtained with moorLDI Laser Doppler Imager (Moor Instruments Ltd., England) at the beginning and at the end of the treatment. The measures parameters were: System Type: moorLDI2-HR, Laser: Infrared; Perfusion, Bandwidth: 100 Hz–15 kHz, Scan Speed: 10 ms/pixel, Scan Distance: 33 cm, Image Resolution: 105 × 115, Image Size: 2.3 cm × 2.3 cm, Total Frames: 1.

2.7. Statistic and analysis

All chart data were expressed as mean ± standard deviation (Mean ± SD). Statistical analysis was performed using the Prism 6 software (GraphPad, San Diego, CA, USA) through Student's *t*-test and One-way ANOVA. Statistical significance was detailed in each analysis.

3. Results and discussion

3.1. Synthesis and characterization of the silica system

A fibrous silica-based material was synthetized starting from an appropriate mixture of cetylpyridinium bromide hydrate, urea and TEOS. The fibrous silica-based system was subsequently functionalized with trimethoxysilylpropyldiethylenetriamine and this allowed the incorporation of chlorambucil and folic acid *via* an amido coupling reaction mediated by EDAC. An organotin derivative, namely $Ph_3Sn\{SCH_2CH_2CH_2Si(OEt)_3\}$ (Scheme 1) was supported on the material, by the elimination of ethanol and formation of Si-O-Si bonds with the silica material. The incorporation of the organotin(IV) fragment was carried out in order to study the potential synergistic activity of both cytotoxic agents loaded on the fibrous silica-based material, namely chlorambucil and the organotin(IV) fragment in **FS-DT-Chl-FA-Sn**. We have already successfully demonstrated for other similar silica-based nanodrugs, [20,73] the system incorporates also folic acid as a targeting fragment, in order to improve the selectivity toward this kind of breast cancer cells overexpressing folate receptors. In addition, the material containing only folic acid and the organotin derivate (**FS-DT-FA-Sn**) were also prepared to study and compare the potential synergistic effect with chlorambucil in the studied triple negative breast cancer model.

All the synthesized materials were characterized by different techniques in order to determine and quantify the incorporation of the different therapeutic and targeting moieties and characterize the physical and chemical properties of the final nanosystems.

The fibrous silica nanoparticle **FS** was characterized by transmission electronic microscopy (TEM) in order to study its morphology, particle size and porosity. Fig. 1 shows that **FS** silica materials are composed of fibrous spherical shaped nanoparticles with a homogeneous distribution. The mean size of the nanoparticles is 427.9 ± 20.9 nm. The TEM micrographs of the FS system clearly show that the porosity of this type of silica-based materials is not made up of a hexagonal arrangement of pores and/or channels (as in the case of MSN or SBA-15), but on the arrangement of radially shaped fibrous channels, with an appearance similar to spherical micelles. Furthermore, radial channels are especially visible on the external surface of the spheres, converging toward the centre of the particle.

IR analysis (Fig. 2A) of the starting fibrous material shows the typical signals corresponding to silica-based materials, namely, the vibration associated to the Si-OH groups at 3400, 1650 and 800 cm^{-1}, and the bands due to the Si–O–Si bonds at 1100 and at 450 cm^{-1}. After functionalization with the DT ligand, additional signals were observed: *ca.* 3200 cm^{-1} assigned to C–N vibrations of primary and secondary amines, at 2950 cm^{-1} due to alkane stretching vibrations ($–CH_3$ pending groups) and at 2850 cm^{-1} ($–CH_2–$ groups). In addition, a low intensity band was observed at *ca.* 1460 cm^{-1}, which corresponds to the vibration of the secondary amines (–NH–) of the ligand. Finally, at 1380 cm^{-1} another peak for the primary amines ($–NH_3$) was also recorded.

With the incorporation of chlorambucil and folic acid (**FS-DT-Chl-FA**), some of the bands of the spectrum changed compared with **FS-DT**, for example, the signal at *ca.* 2960 cm^{-1} is sharper while a shoulder is observed at 1640 cm^{-1} for the –C–N– bonds present in Chl and FA. These changes are attributed to the formation of the amide bonds. When MP-Sn was incorporated on the silica (**FS-DT-Chl-FA-Sn**), the peaks situated at around 2960 cm^{-1}, are again modified, and the stretching vibrations of the $–CH_2$-S– groups appear at *ca.* 700 cm^{-1}. Finally, a small shoulder (at *ca.* 570 cm^{-1}) was also observed in the IR spectrum of the material **FS-DT-Chl-FA-Sn** and is due to the stretching vibration of the Sn–C bonds. The other materials show the same characteristics bands associated to the successive functionalizations (see for example Fig. S1 of supplementary material).

The functionalization with the different fragments was also confirmed by diffuse reflectance UV–Vis spectroscopy (DR-UV). The incorporation of DT is observed in the spectra of Fig. 2B with the appearance of a peak at *ca.* 210 nm. After functionalization with folic acid (Fig. S2) and chlorambucil (Fig. 2B), the spectrum showed two additional peaks at *ca.* 300 nm and 370 nm due to the incorporation of both compounds. Finally, in the tin-functionalized materials the spectrum showed an increase of the intensity of the peak at *ca.* 210 nm which

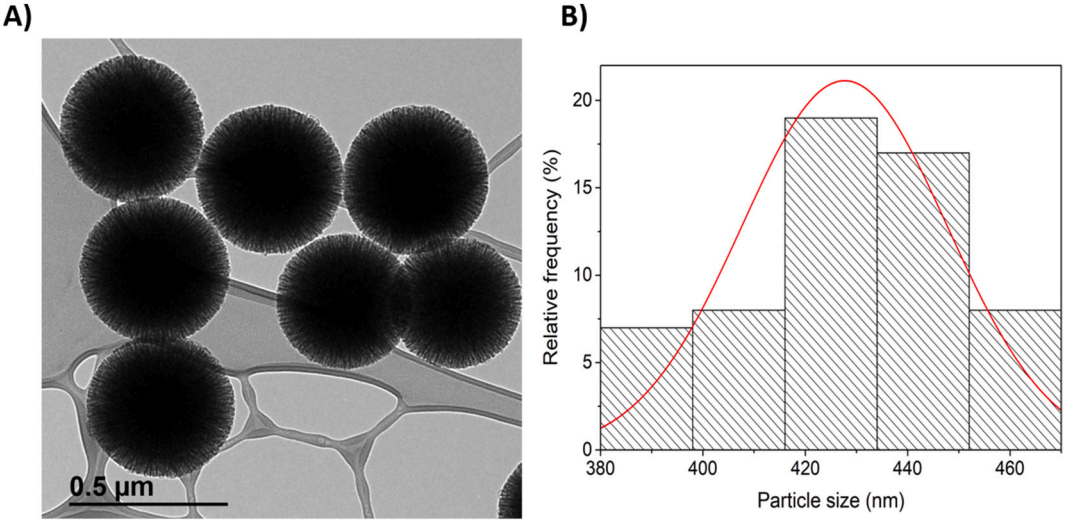

Fig. 1. Characterization of silica nanoparticle by electron microscopy. a) TEM micrograph of fibrous silica particles (FS) and b) particle size distribution.

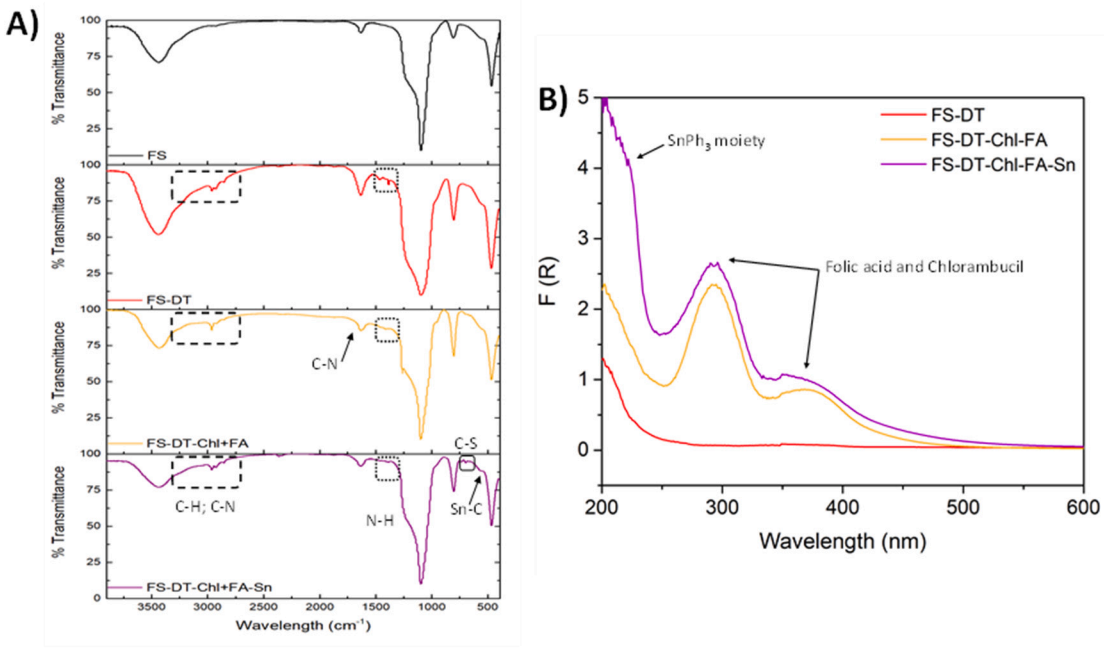

Fig. 2. Characterization of FS surface functionalization by FTIR. (A) IR spectra and (B) diffuse reflectance UV/Vis solid absorption spectra of fibrous silica series.

is probably due to the incorporation of additional aromatic rings of the $SnPh_3$ moiety.

The textural properties of the synthesized materials were determined by nitrogen adsorption-desorption in solids. The results show that **FS** material present a good surface area of 317 m^2/g with a pore volume 0.42 cm^3/g. Upon the successive functionalization reactions of the silica and the incorporation of the different agents, the final tin-functionalized materials, namely **FS-DT-Chl-FA-Sn** showed a decrease in the superficial area (BET surface to 77 m^2/g) and pore volume (0.15 cm^3/g) in comparison with starting material. This behaviour is in agreement with the loading of the different therapeutic and targeting fragments.

The **FS** series (Fig. S3) exhibits an isotherm between type IV and V. Interestingly the **FS** starting material shows a remarkable hysteresis loop between P/P_0 0.1 and 0.8, which indicates the possibility of capillary condensation of the adsorbate and which becomes less evident for the final material **FS-DT-Chl-FA-Sn** which has a lower surface area. The pore size distribution of the starting silicas is shown in Fig. S4A. Because the **FS** porosity is not distributed in homogeneous parallel channels, rather the pore diameter changes as a function of pore depth, two peaks in the size distribution were observed at *ca.* 3.5 and 9.2 nm (Fig. S4A). After functionalization the distribution becomes monomodal with just a maximum at around 9.2 nm, indicating that, some part of the functionalization may be blocking the smaller parts of the channels between fibres, which are usually located close to the centre of the nanoparticles.

In order to quantify the amount of tin-based cytotoxic agent present in each final system, **FS-DT-Chl-FA-Sn** was analyzed by X-ray fluorescence (Table S1). The quantity of tin was 5.13% which is comparable with other systems based on hexagonally distributed porous silica [73]. It is worth noting that, together with the formation of Si-O-Si bonds *via* elimination of ethanol and incorporation of the whole tin compound, a side reaction involving $SnPh_3$ moieties trough the reaction with the silanol groups of the silica material is also possible. This has already been observed in the case of other similar systems based on the incorporation of the organotin compound $Ph_3Sn\{SCH_2CH_2CH_2Si(OEt)_3\}$ [73].

The quantification of folic acid and chlorambucil was carried out by thermogravimetric analysis between 120 and 650 °C (Fig. S5 and Table S2). The incorporation of the polyamine ligand DT is about 0.53 mmol per gram of silica (12.36% in mass), and comparable with other ligands functionalized in silica-based systems [73]. The incorporation of chlorambucil and folic acid *via* carbodiimide coupling corresponds to a weight loss of *ca.* 7–8%. By analyzing the amount of Cl in the final **FS-DT-Chl-FA-Sn** material (Table S1), the quantity of chlorambucil was estimated to be 36.42 mmol/g and consequently, the amount of FA to be 0.08 mmol/g (Table S2).

The final fibrous material was also characterized by ^{13}C CP MAS spectroscopy (Fig. 3A) and ^{29}Si MAS NMR (Fig. 3B). The ^{13}C spectrum shows a set of signals between 0 and 60 ppm assigned to the aliphatic carbons of the DT and MP ligands. Thus, the signals between 0 and 30 ppm are due to the alkyl chains of the ligands, while the signals between 38 and 50 ppm are due to the carbon atoms of the methoxy (from DT) or ethoxy groups (from MP). Interestingly the signal at 38 ppm seems to be more intense probably due to the overlap with the C atom adjacent to that of the C-COR amide bond associated with the incorporation of chlorambucil and folic acid. In addition, the DT ligand shows another signal assigned to $Si\text{-}CH_2\text{-}CH_2\text{-}\underline{C}H_2\text{-}N$ at 50 ppm. Finally, a set of signals between 140 and 160 ppm in **FS–DT-Chl-FA** were assigned to the alkenylic carbon atoms $\underline{C}H{=}\underline{C}H$ from chlorambucil and folic acid. Although of lower intensity, these signals were also observed in the final material **FS-DT-Chl-FA-Sn** together with a set of signals between 120 and 140 ppm, which were assigned to the aromatic carbons of the triphenyl moieties.

All the ^{29}Si MAS NMR spectra of the FS based materials (Fig. 3B) show the typical signals of the Si atoms of porous silica. The more intense peak at *ca.* −110 ppm corresponds to the Q^4 peak [Si_4], while two shoulders at *ca.* −101 ppm and at −90 ppm are due to Q_3 [$Si_3(OH)$] and Q_2 [$Si_2(OH)_2$] silicon atoms, respectively. After the successive functionalization, the intensity of the Q peaks slightly decreases without influencing the silicon framework of the starting particles. In **FS-DT, FS-DT-Chl-FA** and **FS-DT-Chl-FA-Sn** a set of two T peaks were observed at *ca.* -67 ppm (associated with T^3 peak [$(SiO)_3Si\text{-}R$)]) and at ca. −58 ppm (T^2 peak [$(SiO)_2SiOH\text{-}R$)]).

In order to determine the potential mechanism of action of the synthesized materials specifically assessing their ability to act as "classical" or "non-classical" drug delivery systems (releasing or not releasing the metallodrug into the physiological medium) [41,46,47,73,74], the tin-containing material **FS-DT-Chl-FA-Sn** was incubated in PBS medium at 37 °C at different time intervals. In all cases, the quantity of tin-

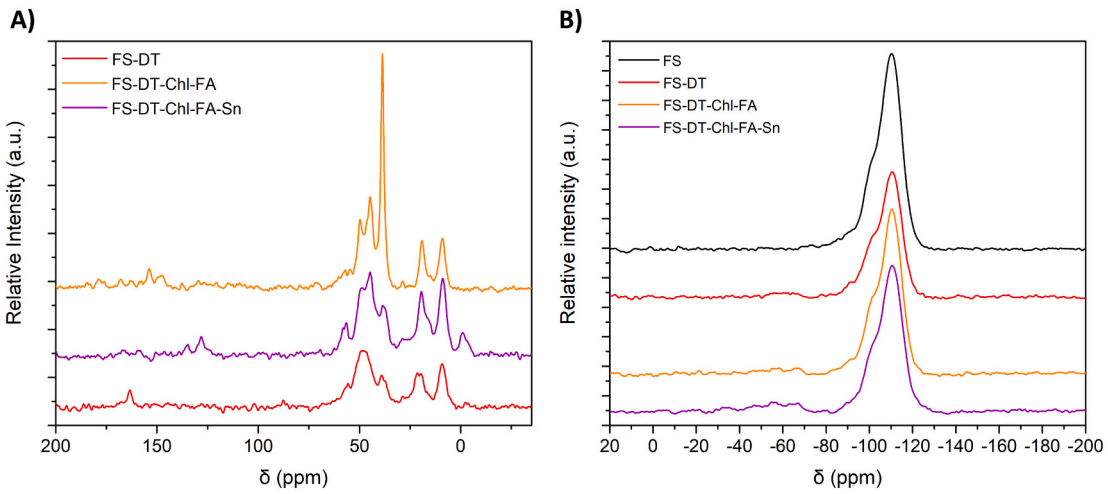

Fig. 3. ^{13}C NMR (A) and ^{29}Si NMR (B) spectra of fibrous silica series.

containing soluble species was less than 0.1 ppm, which corresponds to a release of less than 0.01% of the loaded tin (Table S3). These results indicate that, the materials studied here act as "non-classical" drug-delivery systems, confirming that they do not need to release the metallodrug to be cytotoxic as they act as a whole unit in the studied release period. It is important to note that in previous studies of our research team have demonstrated that the release of a substantial quantity of soluble tin-containing species only occurs after decomposition of the nanoparticle in the biological medium which usually takes more than 15 days.

Finally, we analyzed the hydrodynamic size and isoelectric point of the final nanomaterials by Dynamic Light Scattering technique. Obtained values indicate a good size homogeneity (low polydispersity index) and an elevated surface ζ-potential at physiological pH (isoelectric point >8) in all cases (Table S4). Therefore, a good colloidal stability of **FS-DT-Chl-FA-Sn** in physiological environment -a crucial parameter for *in vivo* applications- is expected.

3.2. *In vitro characterization of the different silica-based multifunctional nanomaterials*

After the physicochemical characterization of the silica materials, their therapeutic capability was analyzed *in vitro*. To study the dose-depending cytotoxicity of all the silica materials, the MTT cell viability assay was carried out using human breast cancer cells (MDA-MB-231). As expected, Sn-functionalized **FS** materials showed higher dose dependent toxicity than silica materials bearing only chlorambucil drug (Fig. 4). The IC_{50} values (the concentration of the drug that reduced cell viability by half) for the materials was calculated 0.84, 0.88 and 0.81 μM for **FS-DT-Chl-FA-Sn**, **FS-DT-Chl-FA** and **FS-DT-FA-Sn** nanodrugs, respectively (Table S5).

After analyzing the antiproliferative activity, we decided to also carry out the wound healing assay or the assessment of the potential of our nanomaterials to inhibit the migration ability of MDA-MB-231 cancer cells. This is a standard *in vitro* technique that evaluates the cell migration behaviour as a marker of the potential ability of cancer cells to migrate within the body and generate cancer metastasis [20,75–77]. To carry out this study, different concentrations between 1 and 25 μM of all the synthesized materials were tested (Fig. S6). The results, reported as relative inhibition percentage, were calculated by the comparison between the scar areas before and after 24 h of incubation with each nanomaterial. Representative results are reported in Fig. 5. As a general consideration, at all the concentrations studied, the bare FS material did not show inhibition of the migration activity whereas the Sn-functionalized material showed higher antimigration

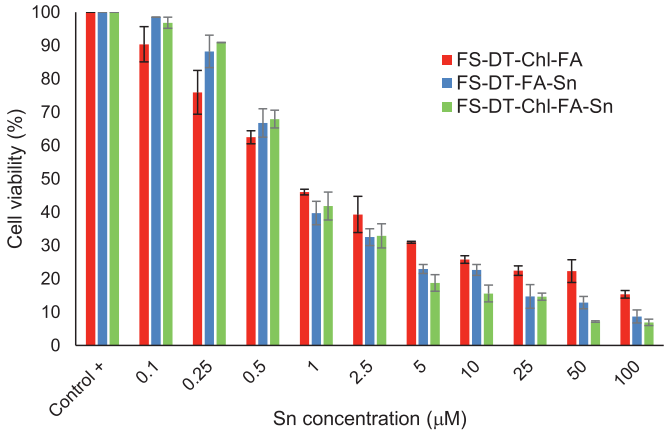

Fig. 4. Viability assay of MDA-MB-231 cells upon incubation with the three different final materials at different concentrations. The results are expressed as % of retained viability in comparison with the control (mean ± SD, n = 3 independent experiments and 3 replicates for each experiment).

properties in comparison with Chl-functionalized nanodrug (Fig. 5). Interestingly, when combined together, both drugs showed a good synergistic effect especially at the lowest concentration (1 μM), with the cells treated individually with **FS-DT-Chl-FA** or **FS-DT-Sn-FA** retaining a 56% and 41% migration ability, respectively. Interestingly, when treated at the same concentrations of combined **FS-DT-Chl-FA-Sn** nanodrug, this value dropped to 22%.

3.3. *In vivo evaluation of silica-based multifunctional metallodrugs on breast adenocarcinoma mouse model*

After the *in vitro* evaluation of the silica nanomaterials, we assessed its theranostic capability *in vivo* by using human breast adenocarcinoma bearing mice. These were randomized in four different groups (n = 4/group) to compare the therapeutic activity of Sn *vs* that of Chl, and to elucidate the potential synergistic therapeutic activity as result of the combination of both drugs. Following a successful dose regimen scheme already studied for the management of this kind of tumour [20,35,63,71,72], the different nanodrugs were administered by means of 6 systemic doses in the tail vein during 13 days.

The diagnostic properties were evaluated by *in vivo* fluorescence imaging 2 h post injection of each dose (Fig. 6). This precise timeframe corresponds to the highest absorbance (accumulated within the tumour

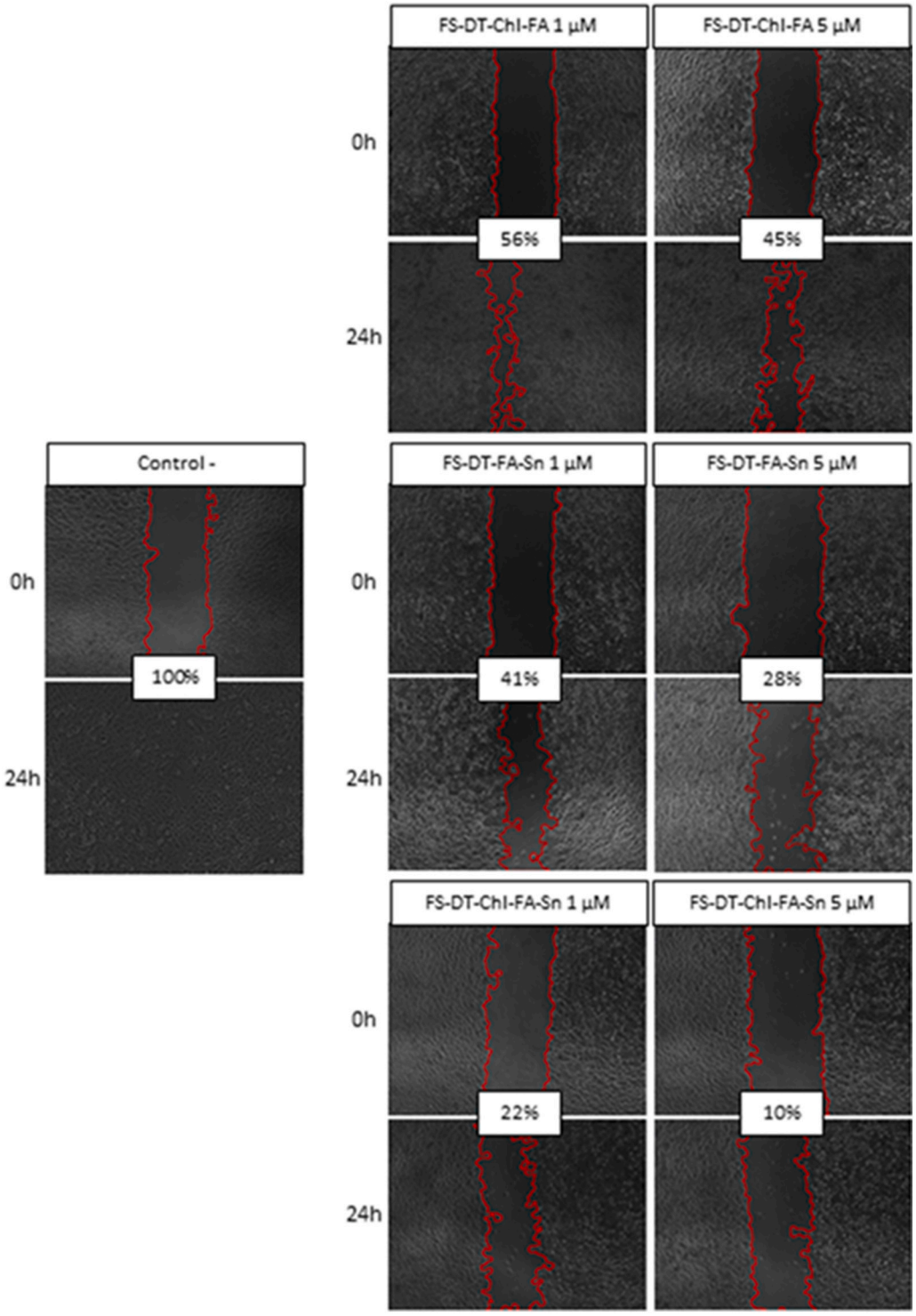

Fig. 5. Migration assay of MDA-MB-231 cells in presence of the final silica nanomaterials. Phase contrast microscopy images where the edges of the scars are marked in red. Negative control (control −): Cells grown in culture media (complete migration and wound healing). (For interpretation of the references to colour in this figure legend, the reader is referred to the web version of this article.)

region) *vs* time ratio observed during the longitudinal follow up of injected mice. These data were also in agreement with similar studies previously carried out and published by our group. [20,35] The representative images of the three mouse groups treated with each different silica materials (**FS-DT-Chl-FA**, **FS-DT-FA-Sn** and **FS-DT-Chl-FA-Sn**) showed the uptake within the tumour area (white arrows) as well as in the liver, in the bowel and to a lesser extent in the bladder, thus, confirming the principal excretion routes.

The therapeutic properties of each nanoformulation were evaluated by measuring the tumour mass growth during the whole treatment. In order to minimize the intrinsic variability within all generated tumours and permit the comparison of the different therapeutic effects of each applied nanosystem *vs* the control group, the results were described as the relative volume increase of each tumour mass at each time point and normalized according to their initial tumour mass at the beginning of the treatment (Fig. 7A). Upon nanodrug treatment, the tumour mass of mice

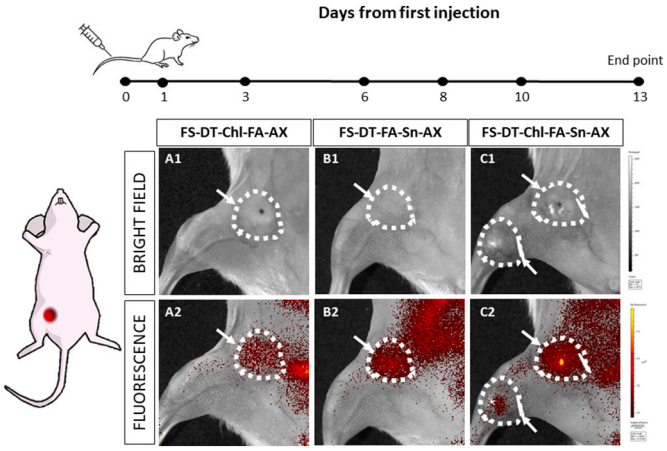

Fig. 6. *In vivo* fluorescence imaging of the mice treated with the three different silica-based nanomaterials (n = 4/group). Row 1 (A1, B1 and C1) corresponds to the bright field images (tumour area is indicated with white arrows) and row 2 (A2, B2 and C2) corresponds to related fluorescence images. Images have been acquired 2 h post-injection of nanoparticles.

treated with saline (control group) increased by 3.8 fold in comparison with their volume measured at the beginning. The tumour volumes of mice treated with **FS-DT-Chl-FA** and **FS-DT-FA-Sn** nanoparticles increased around 2.8 fold in both cases, thus showing antitumoural activity of each nanodrug. As expected, when administered together with the same FS-based nanocarrier, a synergistic antitumour effect can be induced. In fact, after 13 days of therapy, the tumour mass of mouse group treated with **FS-DT-Chl-FA-Sn** increased only 1.8 fold in comparison with their initial volume (Fig. 7B).

After the sacrifice and necropsy of each mouse group, we directly analyzed the *ex vivo* tumour masses. The images of excised tumours proceeding by each group (control, **FS-DT-Chl-FA**, **FS-DT-FA-Sn** and **FS-DT-Chl-FA-Sn**) at endpoint and reported in Fig. 7B clearly confirms our previous results.

Due to its ability to analyze tissue perfusion, we also carried out laser Doppler perfusion imaging (LDI) in order to visualize the impact on the tumour functionality during the *in vivo* therapeutic treatment with the different synergistic FS-based nanodrugs (Fig. 8) [78]. In fact, it is well known that there is a direct relationship between tissue vitality and tissue perfusion. Consequently, the application of LDI in the observation of tissue perfusion of tumour masses may lead to a better understanding of its evolution, therefore, being especially useful during *in vivo* therapeutic experiments. Upon a qualitative analysis of perfusion images (Fig. 8), a great blood flow reduction of tumour treated with **FS-DT-Chl-FA-Sn** (Fig. 8I) was observed in comparison with the saline control group (Fig. 8D). In fact, in addition to the low perfused central necrotic area, even the peripheral zones of tumour mass (generally acknowledged as the most active because of the neoangiogenesis mechanism) showed poor perfusion. On the other hand, the control tumour showed high perfusion activity of both central and peripheral areas, thus, confirming the intense functionality of untreated tumours. Under a quantitative point of view, in the case of untreated tumour, at the end of the study the mean blood flow was retained almost entirely being around 90% of the tumour vascularization observed at the beginning of nanotherapy (Fig. 8E). The tumour treated with **FS-DT-Chl-FA-Sn** showed a great mean blood flux decrease of 60% approx. (Fig. 8J). These results clearly indicate a selective antiangiogenic activity of our multifunctional nanoplatform and they are in agreement with the mass growth reduction previously presented. Altogether, these results confirm the strong antitumoural activity of our multitherapeutic silica-based nanodrugs.

Considering the toxicity concerns related to the use of both chemotherapeutic drugs, the *in vivo* toxicity of the theranostic nanoparticles was analyzed during the entire therapeutic scheme by monitoring the possible impact on the liver and kidney functionality. In fact, as previously showed with *in vivo* imaging experiments (Fig. 6), these two organs have been identified as the principal excretion routes. Toward this scope and because of their usefulness as indicators of hepatic and renal functionalities [79,80], the serum levels of alanine aminotransferase (ALT), aspartate aminotransferase (AST), alkaline phosphatase (AKP), albumin (ALB) and blood urea nitrogen (BUN) were monitored by biochemical assays in serum samples withdrawn at the beginning and at the end of each nanotherapy (Fig. 9). In fact, increased levels of these biomarkers are generally associated to acute and/or chronic liver and kidney injuries. The achieved results (Fig. 9) showed the serum levels of hepatic and renal biomarkers remained constant or slightly decreased at the end of each nanotherapy for almost all the mice groups with exception of **FS-DT-Chl-FA**. In this case, the AKP biomarker indicates a certain hepatic distress at the final point. Nevertheless, when administering the combination of chlorambucil and organotin(IV) metallodrug, the serum level of this hepatic biomarker at the end of the therapy was quite similar to the basal value, thus showing that no hepatic or renal damages had been generated. Interestingly, these *in vivo* results indicate that this synergistic strategy is able to maintain the anticancer activity of chlorambucil and metallodrugs while reducing their intrinsic toxicities (Fig. 9).

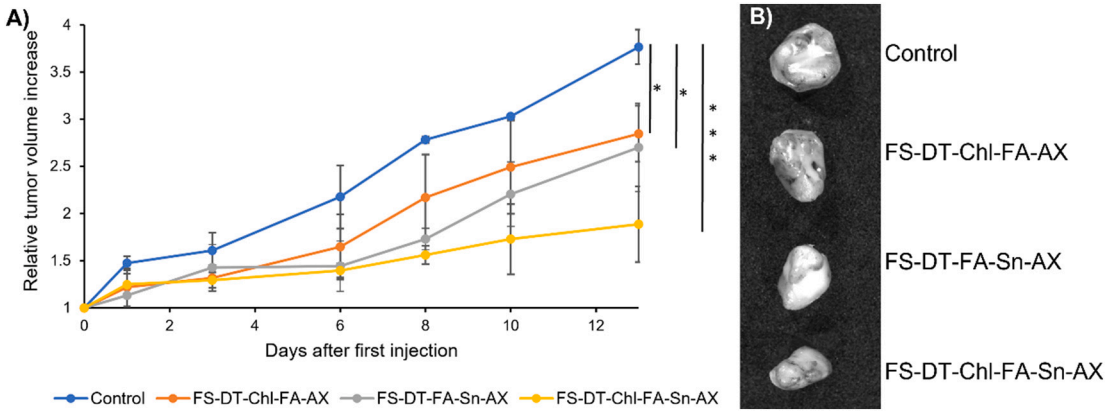

Fig. 7. Evaluation of synergistic antitumour activity of theranostic nanoplatform in TNBC mice models (n = 4/group). (A) Relative tumour volume increase during the treatment with the nanoparticles or placebo (control). (B) *Ex vivo* tumour images for all mice treated with silica nanoparticles or placebo. Significance was calculated by unpaired *t*-test of one-way ANOVA. *: $p < 0.05$ or significant statistical difference between the groups of data; ***: $p < 0.001$ or highly significant statistical difference between the groups of data.

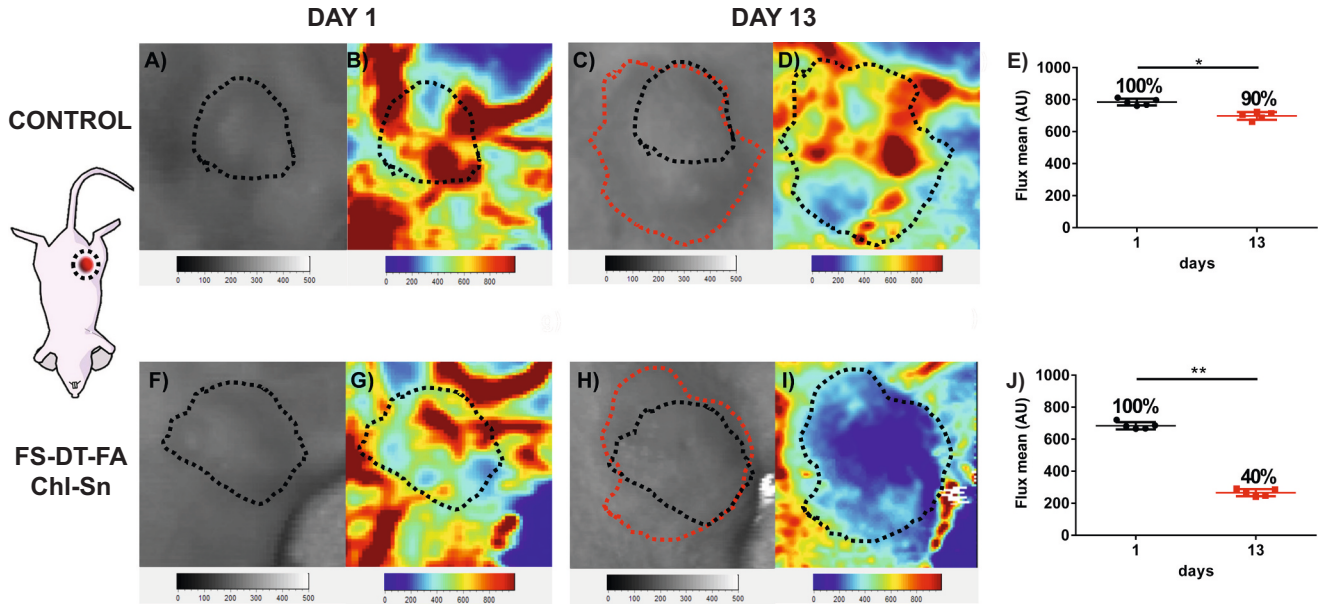

Fig. 8. Laser Doppler perfusion imaging (LDI) of tumour areas (n = 4/group). A) bright field image of control mouse, day 1 (black dotted line: tumour area at the beginning); B) laser Doppler imaging of control mouse, day 1; C) bright field image of control mouse, day 13 (red dotted line: tumour area at the endpoint); D) laser Doppler imaging of control mouse, day 13; E) comparison of blood perfusion in tumour area of control mouse; F) bright field image of treated mouse, day 1 (black dotted line: tumour area at the beginning); G) laser Doppler imaging of treated mouse, day 1; H) bright field image of treated mouse, day 13 (red dotted line: tumour area at the endpoint); I) laser Doppler imaging of treated mouse, day 13; J) comparison of blood perfusion in tumour area of treated mouse. Significance was calculated by unpaired Student *t* test. *: $p < 0.05$ or significant statistical difference between the groups of data; **: $p < 0.01$ or highly significant statistical difference between the groups of data. (For interpretation of the references to colour in this figure legend, the reader is referred to the web version of this article.)

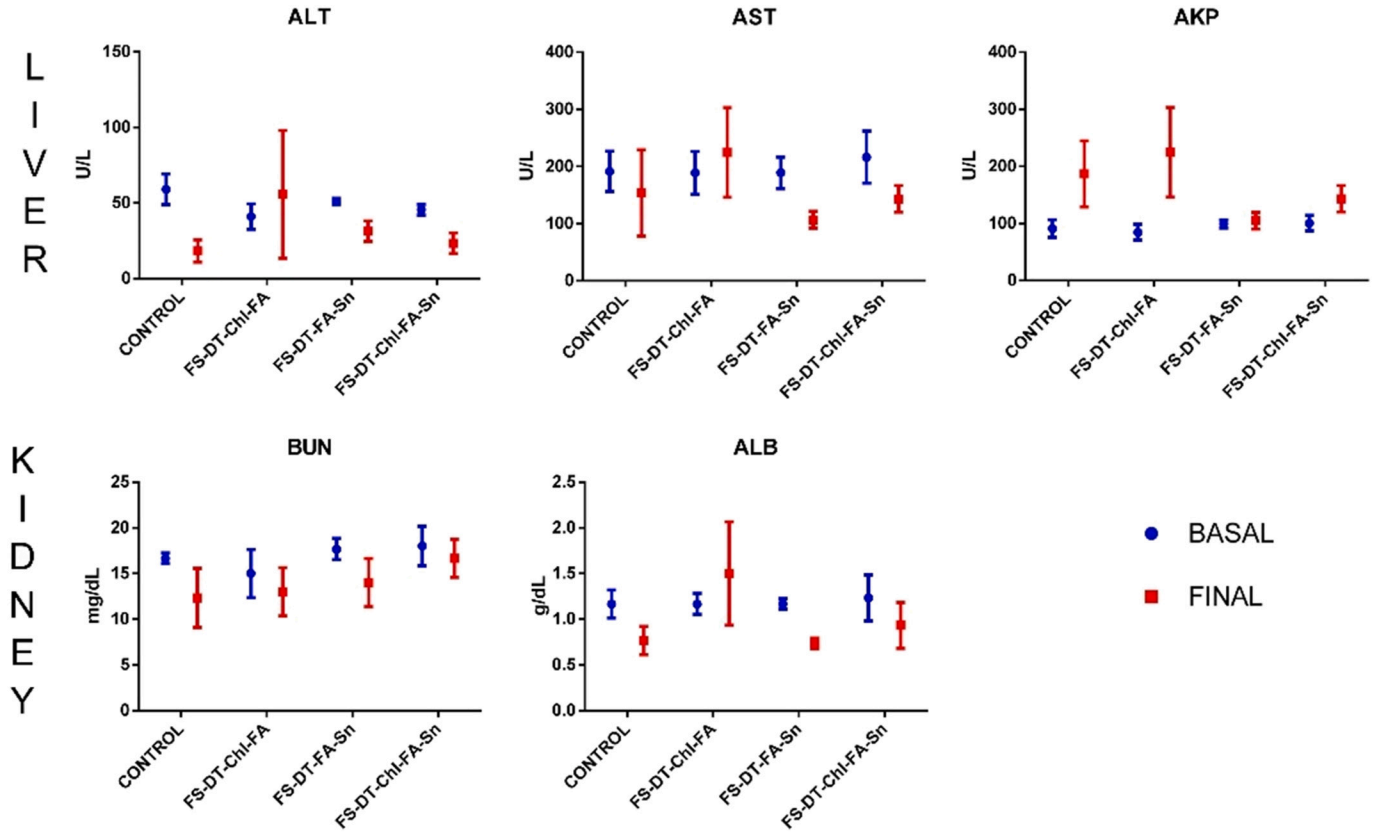

Fig. 9. Serum levels of alanine aminotransferase (ALT), aspartate aminotransferase (AST), alkaline phosphatase (AKP), albumin (ALB) and blood urea nitrogen (BUN) before (blue) and after (red) 13 days of different nanotherapies (n = 4/group). (For interpretation of the references to colour in this figure legend, the reader is referred to the web version of this article.)

4. Conclusions

All together, these results demonstrate the highly promising theranostic activity of our fibrous silica-based nanoplatform against breast cancer in mouse models. In fact, thanks to the targeting moiety FA, the synthesized nanomaterials accumulate selectively within the tumour area after a systemic administration (drug targeting ability); because of the NIRF dye, the nanoplatform can be easily visualized and followed up by *in vivo* fluorescence imaging (diagnostic activity); finally, due to the synergistic effect of chlorambucil and tin based metallodrug, an enhanced therapeutic activity against human breast adenocarcinoma has been successfully induced (multitherapeutic activity). Furthermore, as additional result of our synergistic strategy based on the application of the multifunctional fibrous silica particles, the intrinsic toxicity of chlorambucil has been also reduced, thus, allowing to reduce the limitation related to its use in sub-optimal doses with a consequent treatment inefficiency. All these interesting features have been gathered thanks to the intrinsic properties of the fibrous architecture of the silica particles. In fact, due to their synthetic flexibility and adaptability to many different functionalization behaviours, these siliceous nanoplatforms have clearly demonstrated a great potential for their feasibility as advanced multifunctional nanocarriers in nanomedicine. Furthermore, based on these promising results, future studies of our teams will now be focused mainly on the optimization of the physical properties of the nanoparticles, especially toward the reduction of particle size in order to improve the biodistribution and the tumour-targeting.

Significance of this work

A multifunctional platform based on fibrous silica nanoparticles enabling targeted TNBC cancer therapy and diagnosis is presented.

Thanks to the design of the biomaterial, the *in vivo* targeted functional imaging (by *in vivo* fluorescence and Laser Doppler Imaging) and synergistic multimodal therapy (by 2 different chemotherapeutics) is promoted.

Beside the therapeutic and diagnostic ability, the concomitant side toxicity reduction during TNBC treatment is achieved.

Availability of data and materials

The data generated or analyzed during this study are included in the manuscript and the supplementary information files.

Ethics approval

Mice were housed in specific facilities (pathogen-free for mice) at the Spanish National Centre for Cardiovascular Research (CNIC, Madrid, Spain). All animal experiments were carried out after previous approval by the ethics and animal welfare committee at CNIC and were in agreement with the Spanish Legislation and UE Directive 2010/63/EU.

Consent for publication

The corresponding authors of this manuscript, Marco Filice and Santiago Gómez-Ruiz, on behalf of all co-authors declare the consent of publication of this manuscript in the Journal Biomaterials Advances. All authors have read and approved the submitted final version.

CRediT authorship contribution statement

Karina Ovejero Paredes: Investigation, Data curation, Writing – original draft, Formal analysis, Validation. **Diana Díaz-García:** Investigation, Data curation, Writing – original draft, Formal analysis, Validation. **Irene Mena-Palomo:** Investigation, Data curation, Validation. **Marzia Marciello:** Investigation, Data curation, Formal analysis, Validation. **Laura Lozano Chamizo:** Investigation, Data curation, Validation. **Yurena Luengo Morato:** Investigation, Data curation, Validation. **Sanjiv Prashar:** Writing – original draft, Formal analysis, Validation. **Santiago Gómez-Ruiz:** Conceptualization, Supervision, Writing – original draft, Formal analysis, Writing – review & editing, Validation. **Marco Filice:** Conceptualization, Supervision, Writing – original draft, Formal analysis, Writing – review & editing, Validation.

Declaration of competing interest

None of the authors has any conflicts of interest.

Acknowledgments

We would like to thank the funding of the Ministerio de Ciencia e Innovación of Spain (former Ministerio de Ciencia Innovación y Universidades of Spain) and FEDER, Una manera de hacer Europa for the grant number RTI2018-094322-B-I00. We would also like to thank Comunidad de Madrid for the predoctoral grant PEJD-2017-PRE/BMD-3512 (I.M.-P.). M.M, Y.L.M., and M.F. are grateful to the Comunidad Autónoma de Madrid and FEDER for the I + D collaborative Programme in Biomedicine NIETO-CM (Project reference B2017-BMD3731). M.F. and K.O.P. thank the Comunidad Autónoma de Madrid for research project No. 2017-T1/BIO-4992 ("Atracción de Talento" Action) cofunded by Universidad Complutense de Madrid. M.F is grateful to Instituto de Salud Carlos III (ISCIII) for project No DTS20/00109 (AES-ISCIII). M. M., M.F. and L.L.C would also like to thank Comunidad de Madrid for the predoctoral grant IND2020/BIO-17523. M.F. and K.O.P. acknowledge the support of Microscopy & Dynamic Imaging Unit of CNIC, Madrid, Spain. The Unit is part of the ReDiB-ICTS and has the support of FEDER, "Una manera de hacer Europa." The CNIC is supported by the Instituto de Salud Carlos III (ISCIII), the Ministerio de Ciencia e Innovación (MCIN) and the Pro CNIC Foundation, and is a Severo Ochoa Center of Excellence (grant CEX2020-001041-S funded by MICIN/AEI/10.13039/501100011033)

Appendix A. Supplementary data

Supplementary data to this article can be found online at https://doi.org/10.1016/j.bioadv.2022.212823.

References

[1] J. Zhang, Z. Ye, Y. Lou, Metabolism of chlorambucil by rat liver microsomal glutathione S-transferase, Chem. Biol. Interact. 149 (1) (2004) 61–67, https://doi.org/10.1016/j.cbi.2003.07.002.

[2] M. Schmidt, Chemotherapy in early breast cancer: when, how and which one? Breast Care (Basel) 9 (3) (2014) 154–160, https://doi.org/10.1159/000363755.

[3] S.R. Cummings, J.A. Tice, S. Bauer, W.S. Browner, J. Cuzick, E. Ziv, V. Vogel, J. Shepherd, C. Vachon, R. Smith-Bindman, K. Kerlikowske, Prevention of breast cancer in postmenopausal women: approaches to estimating and reducing risk, J. Natl. Cancer Inst. 101 (6) (2009) 384–398, https://doi.org/10.1093/jnci/djp018.

[4] H. Joensuu, J. Gligorov, Adjuvant treatments for triple-negative breast cancers, Ann. Oncol. 23 (Suppl. 6) (2012) vi40–vi45, https://doi.org/10.1093/annonc/mds194.

[5] W.Y. Kuo, L. Hwu, C.Y. Wu, J.S. Lee, C.W. Chang, R.S. Liu, STAT3/NF-kappaB-regulated lentiviral TK/GCV suicide gene therapy for cisplatin-resistant triple-negative breast cancer, Theranostics 7 (3) (2017) 647–663, https://doi.org/10.7150/thno.16827.

[6] P.-E.J.B. Jonas Bergh, A systematic overview of chemotherapy effects in breast cancer, Acta Oncol. 40 (2–3) (2009) 253–281, https://doi.org/10.1080/02841860120784.

[7] W.F. Anderson, P.S. Rosenberg, A. Prat, C.M. Perou, M.E. Sherman, How many etiological subtypes of breast cancer: two, three, four, or more? J. Natl. Cancer Inst. 106 (8) (2014) https://doi.org/10.1093/jnci/dju165.

[8] W. Zhang, M. Feng, G. Zheng, Y. Chen, X. Wang, B. Pen, J. Yin, Y. Yu, Z. He, Chemoresistance to 5-fluorouracil induces epithelial-mesenchymal transition via up-regulation of snail in MCF7 human breast cancer cells, Biochem. Biophys. Res. Commun. 417 (2) (2012) 679–685, https://doi.org/10.1016/j.bbrc.2011.11.142.

[9] A. Pettersson, R.E. Graff, G. Ursin, I.D. Santos Silva, V. McCormack, L. Baglietto, C. Vachon, M.F. Bakker, G.G. Giles, K.S. Chia, K. Czene, L. Eriksson, P. Hall, M. Hartman, R.M. Warren, G. Hislop, A.M. Chiarelli, J.L. Hopper, K. Krishnan, J. Li, Q. Li, I. Pagano, B.A. Rosner, C.S. Wong, C. Scott, J. Stone, G. Maskarinec, N.

F. Boyd, C.H. van Gils, R.M. Tamimi, Mammographic density phenotypes and risk of breast cancer: a meta-analysis, J. Natl. Cancer Inst. 106 (5) (2014), https://doi.org/10.1093/jnci/dju078.
[10] K. Bielawski, A. Bielawska, A. Muszynska, B. Poplawska, R. Czarnomysy, Cytotoxic activity of G3 PAMAM-NH(2) dendrimer-chlorambucil conjugate in human breast cancer cells, Environ. Toxicol. Pharmacol. 32 (3) (2011) 364–372, https://doi.org/10.1016/j.etap.2011.08.002.
[11] M. Fan, X. Liang, Z. Li, H. Wang, D. Yang, B. Shi, Chlorambucil gemcitabine conjugate nanomedicine for cancer therapy, Eur. J. Pharm. Sci. 79 (2015) 20–26, https://doi.org/10.1016/j.ejps.2015.08.013.
[12] D.J.S. Dias, G.A. Joanitti, R.B. Azevedo, L.P. Silva, C.N. Lunardi, A.J. Gomes, Chlorambucil encapsulation into PLGA nanoparticles and cytotoxic effects in breast cancer cell, J. Biophys. Chem. 06 (01) (2015) 1–13, https://doi.org/10.4236/jbpc.2015.61001.
[13] Z.Y. Ma, D.B. Wang, X.Q. Song, Y.G. Wu, Q. Chen, C.L. Zhao, J.Y. Li, S.H. Cheng, J. Y. Xu, Chlorambucil-conjugated platinum(IV) prodrugs to treat triple-negative breast cancer in vitro and in vivo, Eur. J. Med. Chem. 157 (2018) 1292–1299, https://doi.org/10.1016/j.ejmech.2018.08.065.
[14] M. Di Antonio, K.I. McLuckie, S. Balasubramanian, Reprogramming the mechanism of action of chlorambucil by coupling to a G-quadruplex ligand, J. Am. Chem. Soc. 136 (16) (2014) 5860–5863, https://doi.org/10.1021/ja5014344.
[15] N. Kondo, A. Takahashi, K. Ono, T. Ohnishi, DNA damage induced by alkylating agents and repair pathways, J. Nucleic Acids 2010 (2010), 543531, https://doi.org/10.4061/2010/543531.
[16] D.W. Kufe, J.F. Holland, E. Frei, A.C. Society, Cancer Med. 6 (2003). BC Decker.
[17] N. Benitah, L.P. de Lorimier, M. Gaspar, B.E. Kitchell, Chlorambucil-induced myoclonus in a cat with lymphoma, J. Am. Anim. Hosp. Assoc. 39 (3) (2003) 283–287, https://doi.org/10.5326/0390283.
[18] S.T. Hehn, R.T. Dorr, T.P. Miller, Mood alterations in patients treated with chlorambucil, Clin. Lymphoma 4 (3) (2003) 179–182, https://doi.org/10.3816/clm.2003.n.028.
[19] B. Reux, V. Weber, M.J. Galmier, M. Borel, M. Madesclaire, J.C. Madelmont, E. Debiton, P. Coudert, Synthesis and cytotoxic properties of new fluorodeoxyglucose-coupled chlorambucil derivatives, Bioorg. Med. Chem. 16 (9) (2008) 5004–5020, https://doi.org/10.1016/j.bmc.2008.03.038.
[20] K. Ovejero Paredes, D. Diaz-Garcia, V. Garcia-Almodovar, L. Lozano Chamizo, M. Marciello, M. Diaz-Sanchez, S. Prashar, S. Gómez-Ruiz, M. Filice, Multifunctional silica-based nanoparticles with controlled release of organotin metallodrug for targeted theranosis of breast cancer, Cancers (Basel) 12 (1) (2020), https://doi.org/10.3390/cancers12010187.
[21] M.D. Pegram, A. Lipton, D.F. Hayes, B.L. Weber, J.M. Baselga, D. Tripathy, D. Baly, S.A. Baughman, T. Twaddell, J.A. Glaspy, D.J. Slamon, Phase II study of receptor-enhanced chemosensitivity using recombinant humanized anti-p185HER2/neu monoclonal antibody plus cisplatin in patients with HER2/neu-overexpressing metastatic breast cancer refractory to chemotherapy treatment, J. Clin. Oncol. 16 (8) (1998) 2659–2671, https://doi.org/10.1200/jco.1998.16.8.2659.
[22] S. Quici, A. Casoni, F. Foschi, L. Armelao, G. Bottaro, R. Seraglia, C. Bolzati, N. Salvarese, D. Carpanese, A. Rosato, Folic acid-conjugated europium complexes as luminescent probes for selective targeting of cancer cells, J. Med. Chem. 58 (4) (2015) 2003–2014, https://doi.org/10.1021/jm501945w.
[23] G.L. Zwicke, G.A. Mansoori, C.J. Jeffery, Utilizing the folate receptor for active targeting of cancer nanotherapeutics, Nano Rev. 3 (2012), https://doi.org/10.3402/nano.v3i0.18496.
[24] N. Parker, M.J. Turk, E. Westrick, J.D. Lewis, P.S. Low, C.P. Leamon, Folate receptor expression in carcinomas and normal tissues determined by a quantitative radioligand binding assay, Anal. Biochem. 338 (2) (2005) 284–293, https://doi.org/10.1016/j.ab.2004.12.026.
[25] D. Babaer, S. Amara, M. Ivy, Y. Zhao, P.E. Lammers, J.M. Titze, V. Tiriveedhi, High salt induces P-glycoprotein mediated treatment resistance in breast cancer cells through store operated calcium influx, Oncotarget 9 (38) (2018) 25193–25205, https://doi.org/10.18632/oncotarget.25391.
[26] B.M. Necela, J.A. Crozier, C.A. Andorfer, L. Lewis-Tuffin, J.M. Kachergus, X. J. Geiger, K.R. Kalari, D.J. Serie, Z. Sun, A. Moreno-Aspitia, D.J. O'Shannessy, J. D. Maltzman, A.E. McCullough, B.A. Pockaj, H.E. Cunliffe, K.V. Ballman, E. A. Thompson, E.A. Perez, Folate receptor-alpha (FOLR1) expression and function in triple negative tumors, PLoS One 10 (3) (2015), e0122209, https://doi.org/10.1371/journal.pone.0122209.
[27] M. Hammadi, V. Chopin, F. Matifat, I. Dhennin-Duthille, M. Chasseraud, H. Sevestre, H. Ouadid-Ahidouch, Human ether a-gogo K(+) channel 1 (hEag1) regulates MDA-MB-231 breast cancer cell migration through Orai1-dependent calcium entry, J. Cell. Physiol. 227 (12) (2012) 3837–3846, https://doi.org/10.1002/jcp.24095.
[28] N. Gueder, G. Allan, M.S. Telliez, F. Hague, J.M. Fernandez, E.M. Sanchez-Fernandez, C. Ortiz-Mellet, A. Ahidouch, H. Ouadid-Ahidouch, sp(2) -iminosugar alpha-glucosidase inhibitor 1-C-octyl-2-oxa-3-oxocastanospermine specifically affected breast cancer cell migration through Stim1, beta1-integrin, and FAK signaling pathways, J. Cell. Physiol. 232 (12) (2017) 3631–3640, https://doi.org/10.1002/jcp.25832.
[29] A.J. Gomes, P.A. Barbougli, E.M. Espreafico, E. Tfouni, trans-[Ru(NO)$(NH_3)_4$(py)]$(BF_4)_3.H_2O$ encapsulated in PLGA microparticles for delivery of nitric oxide to B16-F10 cells: cytotoxicity and phototoxicity, J. Inorg. Biochem. 102 (4) (2008) 757–766, https://doi.org/10.1016/j.jinorgbio.2007.11.012.
[30] A.J. Gomes, E.M. Espreafico, E. Tfouni, Trans-[Ru(NO)Cl(cyclam)]$(PF_6)_2$ and [Ru (NO)(Hedta)] incorporated in PLGA nanoparticles for the delivery of nitric oxide to B16–F10 cells: cytotoxicity and phototoxicity, Mol. Pharm. 10 (10) (2013) 3544–3554, https://doi.org/10.1021/mp3005534.
[31] C. Wischke, S.P. Schwendeman, Principles of encapsulating hydrophobic drugs in PLA/PLGA microparticles, Int. J. Pharm. 364 (2) (2008) 298–327, https://doi.org/10.1016/j.ijpharm.2008.04.042.
[32] J. Vandervoort, A. Ludwig, Biocompatible stabilizers in the preparation of PLGA nanoparticles: a factorial design study, Int. J. Pharm. 238 (1–2) (2002) 77–92, https://doi.org/10.1016/s0378-5173(02)00058-3.
[33] H. Kranz, R. Bodmeier, A novel in situ forming drug delivery system for controlled parenteral drug delivery, Int. J. Pharm. 332 (1–2) (2007) 107–114, https://doi.org/10.1016/j.ijpharm.2006.09.033.
[34] D.T. Birnbaum, J.D. Kosmala, L. Brannon-Peppas, Optimization of preparation techniques for poly(lactic acid-co-glycolic acid) nanoparticles, J. Nanopart. Res. 2 (2) (2000) 173–181, https://doi.org/10.1023/A:1010038908767.
[35] A. Sanchez, K.Ovejero Paredes, J. Ruiz-Cabello, P. Martinez-Ruiz, J.M. Pingarron, R. Villalonga, M. Filice, Hybrid decorated core@shell janus nanoparticles as a flexible platform for targeted multimodal molecular bioimaging of cancer, ACS Appl. Mater. Interfaces 10 (37) (2018) 31032–31043, https://doi.org/10.1021/acsami.8b10452.
[36] M. Siccardi, P. Martin, T.O. McDonald, N.J. Liptrott, M. Giardiello, S. Rannard, A. Owen, Nanomedicines for HIV therapy, Ther. Deliv. 4 (2) (2013) 153–156, https://doi.org/10.4155/tde.12.156.
[37] M. Marciello, J. Pellico, I. Fernandez-Barahona, F. Herranz, J. Ruiz-Cabello, M. Filice, Recent advances in the preparation and application of multifunctional iron oxide and liposome-based nanosystems for multimodal diagnosis and therapy, Interface Focus 6 (6) (2016) 20160055, https://doi.org/10.1098/rsfs.2016.0055.
[38] M. Filice, M. Marciello, P.Morales Mdel, J.M. Palomo, Synthesis of heterogeneous enzyme-metal nanoparticle biohybrids in aqueous media and their applications in C-C bond formation and tandem catalysis, Chem. Commun. (Camb.) 49 (61) (2013) 6876–6878, https://doi.org/10.1039/c3cc42475h.
[39] M. Filice, J.M. Palomo, Cascade reactions catalyzed by bionanostructures, ACS Catal. 4 (5) (2014) 1588–1598, https://doi.org/10.1021/cs401005y.
[40] K.S. Lovejoy, S.J. Lippard, Non-traditional platinum compounds for improved accumulation, oral bioavailability, and tumor targeting, Dalton Trans. (48) (2009) 10651–10659, https://doi.org/10.1039/b913896j.
[41] W.A. Wani, S. Prashar, S. Shreaz, S. Gómez-Ruiz, Nanostructured materials functionalized with metal complexes: in search of alternatives for administering anticancer metallodrugs, Coord. Chem. Rev. 312 (2016) 67–98, https://doi.org/10.1016/j.ccr.2016.01.001.
[42] N. Hawkes, Cancer survival data emphasise importance of early diagnosis, BMJ 364 (2019), l408, https://doi.org/10.1136/bmj.l408.
[43] G. Lymperopoulos, P. Lymperopoulos, V. Alikari, C. Dafogianni, S. Zyga, N. Margari, Application of theranostics in oncology, Adv. Exp. Med. Biol. 989 (2017) 119–128, https://doi.org/10.1007/978-3-319-57348-9_10.
[44] M.J. Morris, J.S.D. Bono, K.N. Chi, K. Fizazi, K. Herrmann, K. Rahbar, S.T. Tagawa, L.T. Nordquist, N. Vaishampayan, G. El-Haddad, C.H. Park, T.M. Beer, W.J. Pérez-Contreras, M. Desilvio, E.E. Kpamegan, G. Gericke, R.A. Messmann, B.J. Krause, A. O. Sartor, o.b.o.t.V.T. Investigators, Phase III study of lutetium-177-PSMA-617 in patients with metastatic castration-resistant prostate cancer (VISION), J. Clin. Oncol. 39 (18_suppl) (2021), https://doi.org/10.1200/JCO.2021.39.15_suppl.LBA4. LBA4-LBA4.
[45] R.S. Kalash, V.K. Lakshmanan, C.-S. Cho, I.-K. Park, 4.4 - theranostics, in: M. Ebara (Ed.), Biomaterials Nanoarchitectonics, William Andrew Publishing, 2016, pp. 197–215, https://doi.org/10.1016/B978-0-323-37127-8.00012-1.
[46] C. Bensing, M. Mojic, S. Gómez-Ruiz, S. Carralero, B. Dojcinovic, D. Maksimovic-Ivanic, S. Mijatovic, G.N. Kaluderovic, Evaluation of functionalized mesoporous silica SBA-15 as a carrier system for $Ph_3Sn(CH_2)_3OH$ against the A2780 ovarian carcinoma cell line, Dalton Trans. 45 (47) (2016) 18984–18993, https://doi.org/10.1039/c6dt03519a.
[47] M.Z. Bulatovic, D. Maksimovic-Ivanic, C. Bensing, S. Gómez-Ruiz, D. Steinborn, H. Schmidt, M. Mojic, A. Korac, I. Golic, D. Perez-Quintanilla, M. Momcilovic, S. Mijatovic, G.N. Kaluderovic, Organotin(IV)-loaded mesoporous silica as a biocompatible strategy in cancer treatment, Angew. Chem. Int. Ed. Engl. 53 (23) (2014) 5982–5987, https://doi.org/10.1002/anie.201400763.
[48] J. Ceballos-Torres, S. Prashar, M. Fajardo, A. Chicca, J. Gertsch, A.B. Pinar, S. Gómez-Ruiz, Ether-substituted group 4 metallocene complexes: cytostatic effects and applications in ethylene polymerization, Organometallics 34 (11) (2015) 2522–2532, https://doi.org/10.1021/om5012209.
[49] J. Ceballos-Torres, P. Virag, M. Cenariu, S. Prashar, M. Fajardo, E. Fischer-Fodor, S. Gómez-Ruiz, Anti-cancer applications of titanocene-functionalised nanostructured systems: an insight into cell death mechanisms, Chemistry 20 (34) (2014) 10811–10828, https://doi.org/10.1002/chem.201400300.
[50] S. Gómez-Ruiz, A. Garcia-Penas, S. Prashar, A. Rodriguez-Dieguez, E. Fischer-Fodor, Anticancer applications of nanostructured silica-based materials functionalized with titanocene derivatives: induction of cell death mechanism through TNFR1 modulation, Materials (Basel) 11 (2) (2018), https://doi.org/10.3390/ma11020224.
[51] R.S. Erami, K. Ovejero, S. Meghdadi, M. Filice, M. Amirnasr, A. Rodriguez-Dieguez, M.U. De La Orden, S. Gómez-Ruiz, Applications of nanomaterials based on magnetite and mesoporous silica on the selective detection of zinc ion in live cell imaging, Nanomaterials (Basel) 8 (6) (2018), https://doi.org/10.3390/nano8060434.
[52] D. Perez-Quintanilla, S. Gómez-Ruiz, Z. Zizak, I. Sierra, S. Prashar, I. del Hierro, M. Fajardo, Z.D. Juranic, G.N. Kaluderovic, A new generation of anticancer drugs: mesoporous materials modified with titanocene complexes, Chemistry 15 (22) (2009) 5588–5597, https://doi.org/10.1002/chem.200900151.

[53] V. Shirshahi, M. Soltani, Solid silica nanoparticles: applications in molecular imaging, Contrast Media Mol. Imaging 10 (1) (2015) 1–17, https://doi.org/10.1002/cmmi.1611.
[54] E. Ahmadi, N. Dehghannejad, S. Hashemikia, M. Ghasemnejad, H. Tabebordbar, Synthesis and surface modification of mesoporous silica nanoparticles and its application as carriers for sustained drug delivery, Drug Deliv. 21 (3) (2014) 164–172, https://doi.org/10.3109/10717544.2013.838715.
[55] D. Brevet, M. Gary-Bobo, L. Raehm, S. Richeter, O. Hocine, K. Amro, B. Loock, P. Couleaud, C. Frochot, A. Morere, P. Maillard, M. Garcia, J.O. Durand, Mannose-targeted mesoporous silica nanoparticles for photodynamic therapy, Chem. Commun.(Camb.) (12) (2009) 1475–1477, https://doi.org/10.1039/b900427k.
[56] Y. Chen, Q. Yin, X. Ji, S. Zhang, H. Chen, Y. Zheng, Y. Sun, H. Qu, Z. Wang, Y. Li, X. Wang, K. Zhang, L. Zhang, J. Shi, Manganese oxide-based multifunctionalized mesoporous silica nanoparticles for pH-responsive MRI, ultrasonography and circumvention of MDR in cancer cells, Biomaterials 33 (29) (2012) 7126–7137, https://doi.org/10.1016/j.biomaterials.2012.06.059.
[57] Y. Wang, Q. Zhao, N. Han, L. Bai, J. Li, J. Liu, E. Che, L. Hu, Q. Zhang, T. Jiang, S. Wang, Mesoporous silica nanoparticles in drug delivery and biomedical applications, Nanomedicine 11 (2) (2015) 313–327, https://doi.org/10.1016/j.nano.2014.09.014.
[58] M. Vallet-Regí, A. Ramila, R.P. del Real, J. Pérez-Pariente, A new property of MCM-41: drug delivery system, Chem. Mater. 13 (2001) 308–311.
[59] C.-H. Lee, S.-H. Cheng, Y.-J. Wang, Y.-C. Chen, N.-T. Chen, J. Souris, C.-T. Chen, C.-Y. Mou, C.-S. Yang, L.-W. Lo, Near-infrared mesoporous silica nanoparticles for optical imaging: characterization and in vivo biodistribution, Adv. Funct. Mater. 19 (2) (2009) 215–222, https://doi.org/10.1002/adfm.200800753.
[60] R. Guillet-Nicolas, M. Laprise-Pelletier, M.M. Nair, P. Chevallier, J. Lagueux, Y. Gossuin, S. Laurent, F. Kleitz, M.A. Fortin, Manganese-impregnated mesoporous silica nanoparticles for signal enhancement in MRI cell labelling studies, Nanoscale 5 (23) (2013) 11499–11511, https://doi.org/10.1039/c3nr02969g.
[61] J. Xie, S. Lee, X. Chen, Nanoparticle-based theranostic agents, Adv. Drug Deliv. Rev. 62 (11) (2010) 1064–1079, https://doi.org/10.1016/j.addr.2010.07.009.
[62] L.R. Jaidev, D.R. Chellappan, D.V. Bhavsar, R. Ranganathan, B. Sivanantham, A. Subramanian, U. Sharma, N.R. Jagannathan, U.M. Krishnan, S. Sethuraman, Multi-functional nanoparticles as theranostic agents for the treatment & imaging of pancreatic cancer, Acta Biomater. 49 (2017) 422–433, https://doi.org/10.1016/j.actbio.2016.11.053.
[63] A. Lazaro-Carrillo, M. Filice, M.J. Guillen, R. Amaro, M. Vinambres, A. Tabero, K. O. Paredes, A. Villanueva, P. Calvo, M.Del Puerto Morales, M. Marciello, Tailor-made PEG coated iron oxide nanoparticles as contrast agents for long lasting magnetic resonance molecular imaging of solid cancers, Mater. Sci. Eng. C Mater. Biol. Appl. 107 (2020), 110262, https://doi.org/10.1016/j.msec.2019.110262.
[64] M. Talelli, A. Aires, M. Marciello, Protein-modified magnetic nanoparticles for biomedical applications, Curr. Org. Chem. 19 (2015), https://doi.org/10.2174/1385272819666150810221009, 1-1.
[65] M. Filice, J. Ruiz-Cabello, Nucleic Acid Nanotheranostics: Biomedical Applications, Elsevier, Amsterdam,Netherlands, 2019, https://doi.org/10.1016/C2017-0-01070-4.
[66] C. Huang, T. Ozdemir, L.C. Xu, P.J. Butler, C.A. Siedlecki, J.L. Brown, S. Zhang, The role of substrate topography on the cellular uptake of nanoparticles, J. Biomed. Mater. Res. B Appl. Biomater. 104 (3) (2016) 488–495, https://doi.org/10.1002/jbm.b.33397.
[67] A. Piloni, C.K. Wong, F. Chen, M. Lord, A. Walther, M.H. Stenzel, Surface roughness influences the protein corona formation of glycosylated nanoparticles and alter their cellular uptake, Nanoscale 11 (48) (2019) 23259–23267, https://doi.org/10.1039/c9nr06835j.
[68] L. Li, J. Song, J. Wang, W. Fan, Controllable synthesis of mesoporous silica with hierarchical architecture, Mater. Express 7 (4) (2017) 283–290, https://doi.org/10.1166/mex.2017.1381.
[69] J.A. Flood-Garibay, M.A. Méndez-Rojas, Synthesis and characterization of magnetic wrinkled mesoporous silica nanocomposites containing Fe3O4 or CoFe2O4 nanoparticles for potential biomedical applications, Colloids Surf. A Physicochem. Eng. Asp. 615 (2021), https://doi.org/10.1016/j.colsurfa.2021.126236.
[70] S.M. Sadeghzadeh, R. Zhiani, S. Emrani, Pd/APTPOSS@KCC-1 as a new and efficient support catalyst for C-H activation, RSC Adv. 7 (40) (2017) 24885–24894, https://doi.org/10.1039/C7RA03698A.
[71] J.M. Rosenholm, V. Mamaeva, C. Sahlgren, M. Linden, Nanoparticles in targeted cancer therapy: mesoporous silica nanoparticles entering preclinical development stage, Nanomedicine (London) 7 (1) (2012) 111–120, https://doi.org/10.2217/nnm.11.166.
[72] E. Li, Y. Yang, G. Hao, X. Yi, S. Zhang, Y. Pan, B. Xing, M. Gao, Multifunctional magnetic mesoporous silica nanoagents for in vivo enzyme-responsive drug delivery and MR imaging, Nanotheranostics 2 (3) (2018) 233–242, https://doi.org/10.7150/ntno.25565.
[73] D. Diaz-Garcia, K. Montalban-Hernandez, I. Mena-Palomo, P. Achimas-Cadariu, A. Rodriguez-Dieguez, E. Lopez-Collazo, S. Prashar, K. Ovejero Paredes, M. Filice, E. Fischer-Fodor, S. Gómez-Ruiz, Role of folic acid in the therapeutic action of nanostructured porous silica functionalized with organotin(IV) compounds against different cancer cell lines, Pharmaceutics 12 (6) (2020), https://doi.org/10.3390/pharmaceutics12060512.
[74] D. Díaz-García, L. Sommerova, A. Martisova, H. Skoupilova, S. Prashar, T. Vaculovic, V. Kanicky, I. del Hierro, R. Hrstka, S. Gómez-Ruiz, Mesoporous silica nanoparticles functionalized with a dialkoxide diorganotin(IV) compound: in search of more selective systems against cancer cells, Microporous Mesoporous Mater. 300 (2020), https://doi.org/10.1016/j.micromeso.2020.110154.
[75] T. Fujisawa, B. Rubin, A. Suzuki, P.S. Patel, W.A. Gahl, B.H. Joshi, R.K. Puri, Cysteamine suppresses invasion, metastasis and prolongs survival by inhibiting matrix metalloproteinases in a mouse model of human pancreatic cancer, PLOS ONE 7 (4) (2012), e34437, https://doi.org/10.1371/journal.pone.0034437.
[76] J. Hai, C.Q. Zhu, B. Bandarchi, Y.H. Wang, R. Navab, F.A. Shepherd, I. Jurisica, M. S. Tsao, L1 cell adhesion molecule promotes tumorigenicity and metastatic potential in non-small cell lung cancer, Clin. Cancer Res. 18 (7) (2012) 1914–1924, https://doi.org/10.1158/1078-0432.CCR-11-2893.
[77] N. Lecomte, J.T. Njardarson, P. Nagorny, G. Yang, R. Downey, O. Ouerfelli, M. A. Moore, S.J. Danishefsky, Emergence of potent inhibitors of metastasis in lung cancer via syntheses based on migrastatin, Proc. Natl. Acad. Sci. U. S. A. 108 (37) (2011) 15074–15078, https://doi.org/10.1073/pnas.1015247108.
[78] D.L. Liu, K. Svanberg, I. Wang, S. Andersson-Engels, S. Svanberg, Laser doppler perfusion imaging: new technique for determination of perfusion and reperfusion of splanchnic organs and tumor tissue, Lasers Surg. Med. 20 (4) (1997) 473–479, https://doi.org/10.1002/(sici)1096-9101(1997)20:4<473::aid-lsm15>3.0.co;2-c.
[79] R.J. Church, P.B. Watkins, Serum biomarkers of drug-induced liver injury: current status and future directions, J. Dig. Dis. 20 (1) (2019) 2–10, https://doi.org/10.1111/1751-2980.12684.
[80] B.R. Griffin, S. Faubel, C.L. Edelstein, Biomarkers of drug-induced kidney toxicity, Ther. Drug Monit. 41 (2) (2019) 213–226, https://doi.org/10.1097/FTD.0000000000000589.